Research Square

Preprints are preliminary reports that have not undergone peer review.
They should not be considered conclusive, used to inform clinical practice,
or referenced by the media as validated information.

Biological carbon accumulation accelerates CO_2 outgassing after abrupt Bering Sea warming

Hung-Wei Shu

hwshu@jamstec.go.jp

Japan Agency for Marine-Earth Science and Technology https://orcid.org/0000-0002-5480-7235

Yosuke Iida

Japan Meteorological Agency https://orcid.org/0000-0001-5711-1375

Akihiko Murata

Japan Agency for Marine-Earth Science and Technology https://orcid.org/0000-0002-5931-2784

Hiroaki Tatebe

Japan Agency for Marine-Earth Science and Technology https://orcid.org/0000-0002-2265-5847

Satoshi Osafune

Global Ocean Observation Research Center, Japan Agency for Marine-Earth Science and Technology

Sayaka Yasunaka

Graduate School of Science, Tohoku University

Shinichiro Kida

Research Institute for Applied Mechanics, Kyushu University https://orcid.org/0000-0002-9471-4316

Shinya Kouketsu

Japan Agency for Marine-Earth Science and Technology https://orcid.org/0000-0002-8217-5888

Article

Keywords:

Posted Date: November 16th, 2026

DOI: https://doi.org/10.21203/rs.3.rs-11690736/v1

License: This work is licensed under a Creative Commons Attribution 4.0 International License.
Read Full License

Additional Declarations: There is **NO** Competing Interest.

Biological carbon accumulation accelerates CO_2 outgassing after abrupt Bering Sea warming

Hung-Wei Shu[1*], Yosuke Iida[2], Akihiko Murata[3], Hiroaki Tatebe[1,4], Satoshi Osafune[3], Sayaka Yasunaka[4,5], Shinichiro Kida[6] and Shinya Kouketsu[3,4]

1. Research Center for Environmental Modeling and Application, Japan Agency for Marine-Earth Science and Technology, Yokohama, 236-0001, Japan.
2. Global Environment and Marine Department, Japan Meteorological Agency, 1-3-4 Otemachi Chiyoda-ku, Tokyo, 100-8122, Japan
3. Global Ocean Observation Research Center, Japan Agency for Marine-Earth Science and Technology, Yokosuka, 237-0061, Japan.
4. Advanced Institute for Marine Ecosystem Change, Japan Agency for Marine-Earth Science and Technology, Yokohama, 236-0001, Japan
5. Graduate School of Science, Tohoku University, 6-3 Aramaki Aza-Aoba, Aoba-Ku, Sendai, 980-8578, Japan
6. Research Institute for Applied Mechanics, Kyushu University, Kasuga, 816- 8580, Japan.

*Corresponding author: H.W. Shu; E-mail: hwshu@jamstec.go.jp

Abstract

Each winter, deepening of the wintertime mixed layer renews subsurface waters in productive high-latitude seas, regulating duration of regenerated dissolved inorganic carbon (DIC) stored below the surface. However, whether weakening of this winter water-mass renewal allows sustained biological carbon supply to establish a long-term reservoir remains unclear. Here we identify multi-year accumulation of predominantly regenerated carbon in the main basin of the Bering Sea during subsurface warming after 2014, associated with weakened winter water-mass renewal. Repeated shipboard observations reveal a ~56.8 μmol·kg^{-1} increase in DIC at 26.50 σ_θ between 1993 and 2023, more than 70% of which is non-anthropogenic, dominated by regenerated biological carbon. Monthly DIC reconstruction indicates that weakened winter renewal accumulates DIC at ~3.5 μmol·kg^{-1}·year^{-1} after 2014. Atmospheric reanalysis further shows that strengthened Ekman suction due to enhanced wind stress curl after 2018 shoaled carbon-rich density layers and make it intersecting with the wintertime mixed layer, coinciding with winter CO_2 outgassing rising to 1.75 times the pre-2014 mean. These results show that, under sustained biological carbon supply, the long-term regenerated-carbon reservoir established by weakened winter renewal is not necessarily permanent; it can become eruptive CO_2 outgassing source when surface–subsurface connectivity is restored by subsequent shorter-term changes in atmospheric forcing.

1. Introduction

The biological pump continuously exports organic carbon from the surface into the ocean interior, generating dissolved inorganic carbon (DIC) through remineralization. The storage of regenerated carbon depends not only on biological carbon supply but also on how rapidly subsurface waters are renewed through exchange with the surface [1–3]. Each winter, deepening of the mixed layer enhances surface–subsurface exchange, supplying cold surface water downward while entraining DIC-rich subsurface water upward and thereby renewing the properties of the subsurface water masses [4–6]. When this winter water-mass renewal weakens, regenerated carbon can remain isolated below the surface for longer period, allowing sustained biological carbon supply to accumulate in subsurface [6,7].

The main basin of the Bering Sea (hereafter Bering Basin) is a biologically productive subarctic marginal sea connecting the Arctic and North Pacific Oceans (**Fig. 1a**), continually generating the regenerated DIC to its subsurface. The exchange between the eastern Bering Sea shelf and the Bering Basin supplies nutrients along the shelf break, maintaining the highly productive Green Belt [8,9]. This high productivity enhances organic-carbon export to the subsurface, generating regenerated DIC through remineralization [10,11]. During winter, mixed-layer development entrains DIC-rich subsurface water toward the surface, promoting seasonal CO_2 outgassing [11,12]. As winter-renewed water persists into summer, the vertical DIC distribution exhibits a weak gradient above this subsurface layer, becoming markedly steeper below it.

However, whether prolonged weakening of winter water-mass renewal in productive seas can build a multi-year subsurface carbon reservoir remains poorly understood. In the Bering Basin, warm Pacific-origin water enters through Aleutian Straits, flowing along the eastern Bering Sea shelf as the Bering Slope Current [13,14] (**Fig. 1a**). Wintertime mixed-layer development supplies cold surface water to about 26.60 σθ (σθ ≡ potential density – 1000 $kg \cdot m^{-3}$), cooling and renewing the Pacific-origin subsurface water [4,5]. The remnants of this winter-renewed water persist through summer as dichothermal water between the warm surface layer and underlying Pacific-origin mesothermal water. Together with the entrainment of DIC-rich during the winter, this dichothermal water marks the temperature minimum and the transition of vertical DIC gradient at the same time.

Since 2014, the Bering Basin has undergone basin-wide subsurface warming, associated with weakened winter water-mass renewal [15]. Previous observations from 2007–2022 in Bering Basin showed that surface freshening reduced upper-ocean density from early 2010s, strengthening stratification and restricting winter diabatic exchange process. This reduced the downward supply of cold surface water, retaining the Pacific-originated warm water in the subsurface. The warming thus persisted within the 26.40–26.70 σθ density range for nearly a decade, indicating a prolonged weakening of the winter water-mass renewal [15]. Given that winter water-mass renewal also entrains DIC-rich subsurface water toward the surface, how this restricted winter diabatic exchange process observed in the Bering Basin allow the accompanying changes in subsurface carbon storage and later re-expose is unknown.

This study investigates the influences of weakening of winter water-mass renewal on vertical DIC distribution and subsequent re-exposure of DIC in the Bering Basin, hypothesizing that regenerated carbon accumulated alongside subsurface warming. This accumulation may form a multi-year subsurface carbon reservoir that is later re-entrained into the wintertime mixed layer, contributing to enhanced winter CO_2 outgassing. Using repeated biogeochemical observations along the P14 hydrographic section (1993, 2007, and 2023), this study quantifies the changes in DIC and the contributions of non-anthropogenic processes to these changes. An existing data-constrained machine-learning DIC product and an ocean objective-analysis product can resolve the accumulation rate and physical evolution, while atmospheric reanalysis and a regional CO_2 flux product are able to examine the subsequent surface response. By linking biological carbon supply with changes in winter water-mass renewal, this study provides a framework for assessing when weakened winter renewal promotes long-term carbon sequestration and when it instead postpones the return of regenerated carbon to the atmosphere in productive high-latitude oceans.

2. Results

2.1 Sustained subsurface warming and DIC increase

Subsurface warming and a DIC increase were observed along the repeat P14 hydrographic section (hereafter P14 line) across the Bering Basin (**Fig. 1a**). The P14 line follows the Date Line from the North Pacific into the Bering Basin with occupations in 1993, 2007, and 2023 (**Supplementary Fig. S1**), providing a rare multi-decadal biogeochemical record in the region (see Methods) [16–18].

The subsurface warming remained evident in 2023. Both the 1993 and 2007 occupations preceded the 2014 warming transition, with their mean used as the historical baseline (see Methods). This baseline showed a distinct subsurface temperature minimum within the 26.40–26.70 σθ isopycnals (**Fig. 1b**), corresponding to the dichothermal water formed from the remnant wintertime mixed-layer [4,5,15]. By 2023, potential temperature within this density range had increased by up to 1.5 °C relative to the baseline (**Fig. 1c**). The warming remained confined to the former dichothermal-water layer, indicating that the post-2014 subsurface warming had sustained for nearly a decade (**Supplementary Fig. S2**).

Salinity-normalized DIC (nDIC) showed a co-located increase within the same density range. In the historical baseline, nDIC increased gradually with depth, reflecting the DIC-rich deeper waters (**Fig. 1d**). By 2023, nDIC had increased markedly within the 26.40–26.70 σθ isopycnals, reaching more than 50 μmol·kg^{-1} near 26.50 σθ relative to the baseline (**Fig. 1e**). This enrichment overlapped closely with the subsurface warming, indicating a coupled reshaping of the thermal and carbon structures.

To determine whether this nDIC increase reflects atmospheric uptake or internal oceanic processes, a transit-time distribution analysis is applied.

2.2 Regenerated biological carbon dominates the subsurface DIC increase

Both the subsurface warming and DIC increase developed predominantly after 2007. Averaging the observed values north of 52.0 ºN along P14 line as a basin-mean value (vertical dashed line, **Fig. 1b**), anomalies at 26.50 σθ were most pronounced (**Fig. 2**). Potential

120 temperature increased by 1.2 °C at 26.50 σθ from 1993 to 2023, compared with only 0.2 °C
121 from 1993 to 2007 (**Fig. 2a**).

122 Total DIC showed a similar change, increasing by 56.8 ± 16.4 μmol·kg^{-1} at 26.50 σθ
123 from 1993 to 2023, but by only 12.5 μmol·kg^{-1} from 1993 to 2007 (**Fig. 2b**). Noted that
124 unnormalized total DIC is used here because salinity normalization is incompatible with the
125 transit-time distribution method applied below. Most of the observed warming and DIC
126 increase therefore developed within the 2007–2023 interval, encompassing the onset of
127 subsurface warming in 2014.

128 The dominant contribution to this subsurface DIC increase was non-anthropogenic. A
129 transit-time distribution (TTD) analysis assuming an inverse Gaussian distribution was applied
130 by using chemical tracers (see Methods). Anthropogenic carbon (DIC_{ant}) increased by 15.1 ±
131 1.7 μmol·kg^{-1}, accounting for only 26.6% of the total DIC increase (**Fig. 2b**). The remaining
132 41.7 ± 17.3 μmol·kg^{-1}, or 73.3%, was retained as a residual after subtracting DIC_{ant} (**Fig. 2b**).
133 The dominance of the non-anthropogenic residual is robust across the assumed TTD mixing-
134 advection rations (**Supplementary Fig. S3**). This residual includes biological, solubility,
135 circulation, and lateral-transport effects, requiring further attribution before being interpreted
136 as carbon originated from natural climate variability.

137 The residual DIC from the TTD method was dominated by the soft-tissue biological
138 component. This residual was further decomposed using apparent oxygen utilization (AOU) to
139 estimate the soft-tissue contribution, alkalinity changes to estimate the hard-tissue contribution,
140 and carbonate-system calculations to isolate the solubility effect (see Methods). At 26.50 σθ,
141 the soft-tissue component increased by 48.7 ± 19.1 μmol·kg^{-1} from 1993 to 2023, compared
142 with 7.6 μmol·kg^{-1} from 1993 to 2007 **(Fig. 2c).** The hard-tissue component increased by 7.1
143 ± 3.6 μmol·kg^{-1}, whereas the solubility component decreased by −10.0 ± 3.6 μmol·kg^{-1}. The
144 negative solubility contribution indicates that subsurface warming reduced equilibrium DIC,
145 excluding increased solubility as the source of the enrichment.

146 Together, the biological and solubility components yielded 45.8 μmol·kg^{-1}, comparable
147 to the TTD residual of 41.7 μmol·kg^{-1}. The dominant soft-tissue contribution indicates that
148 most of the residual was associated with regenerated biological carbon. Because the AOU-
149 based estimate reflects remineralization and the time elapsed since surface exposure, its
150 increase is also suggesting a reduced water-mass renewal.

The TTD residual is therefore interpreted as predominantly natural-origin carbon, with regenerated biological carbon making the primary contribution, identifying as the dominate source of the subsurface DIC enrichment. An independent monthly DIC product (MOBO-DIC) is then examined to resolve the temporal evolution within 2007–2023.

2.3 Multi-year accumulation of subsurface carbon

MOBO-DIC [19] is an existing data-constrained machine-learning DIC reconstruction product at 1° × 1° spatial resolution covering 2004–2019 (see Method), resolving a progressive increase in subsurface nDIC. Combined with hydrographic fields from the oceanic objective analysis data (ProjD) [20] , the temporal evolution of nDIC along density surfaces was tracked (see Method).

Averaged across the Bering Basin (encircled by the 200-m isobath), potential temperature from ProjD shows sustained warming within the 26.40–26.70 σθ isopycnals from 2014 onward (**Fig. 3a**). Parallelly, MOBO-DIC shows a concurrent increase in nDIC within the same density range (**Fig. 3b**), linking the carbon enrichment to the post-2014 hydrographic transition.

The winter loss of nDIC at 26.50 σθ disappeared after 2014, linking the carbon increase to suppressed winter entrainment (**Fig. 3c**). Averaged over the pre-2014 cold period, nDIC decreased around March–April as the layer was entrained into the wintertime mixed layer (black line, **Fig. 3c**). This seasonal drawdown was largely absent during the post-2014 warm period (red line, **Fig. 3c**), reducing the seasonal amplitude from 14.0 to 10.5 μmol·kg^{-1}. Their difference represents the suppressed wintertime DIC removal, establishing an annual accumulation rate of 3.5 μmol·kg^{-1}·yr^{-1} for the subsurface layer.

This accumulation rate is consistent with the carbon enrichment within MOBO-DIC itself. Annual-mean nDIC increased from 2264.5 ± 5.8 μmol·kg^{-1} during the cold period to 2276.1 ± 4.7 μmol·kg^{-1} during the warm period, yielding a mean difference of 11.6 μmol·kg^{-1}. Scaling this period-mean difference across the full transition (approximately double the period-mean difference) and applying the 73.3% natural-origin fraction gives an accumulated increase of 17.0 μmol·kg^{-1}. Dividing by 3.5 μmol·kg^{-1}·yr^{-1} yields 4.9 years, closely matching the five-year duration from the 2014 warming onset to the end of MOBO-DIC record in 2019.

The same accumulation rate also accounts for the longer-term intensive observed along the P14 line. The non-anthropogenic DIC increase from 1993 to 2023 was 41.7 μmol·kg^{-1}. Dividing this increase by 3.5 μmol·kg^{-1}·yr^{-1} yields an accumulation duration of 11.9 years, closely matching the ~10-year period from the 2014 warming onset to the 2023 occupation. Using the salinity-normalized P14 increase of 37.4 μmol·kg^{-1} (2023–2007, **Supplementary Fig. S2**) gives a comparable timescale of 10.7 years. This agreement across the reconstructed MOBO-DIC record and independent P14 line observations supports progressive subsurface carbon accumulation after 2014.

The vertical profiles further illustrate this transition. In 1993 and 2007, both temperature and DIC showed distinct subsurface minimum and transition point in vertical gradient respectively within the remnant wintertime mixed-layer (**Supplementary Fig. S2**). By 2023, both temperature minimum and DIC vertical gradient transition point had disappeared, replacing with warmer, DIC-enriched water. The loss of the DIC vertical gradient transition point corresponds to the disappearance of the annual winter reset. The 26.50 σθ surface is therefore defined here as the DIC accumulating layer.

This accumulated carbon can influence surface CO_2 flux once the layer reconnects with the wintertime mixed layer. To clarify the mechanism of surface release, the physical processes controlling this re-entrainment are examined next.

2.4 Wind-driven re-entrainment accelerates winter CO_2 outgassing

Enhanced stratification persisted in the Bering Basin after the onset of subsurface warming in 2014. After removing the climatological seasonal cycle, basin-averaged temperature from ProjD remained elevated within the 26.40–26.70 σθ isopycnals, accompanied by an increased Brunt–Väisälä frequency (N^2; **Fig. 4a, b**). These changes persisted through [2023/2024], maintaining the post-2014 stratified state.

After 2018, basin-averaged Ekman suction strengthened (**Fig. 4c**). The Bering Basin is an upwelling-dominated region driven by the positive wind-stress curl of the Aleutian Low [21]. After removing 1998–2022 seasonal cycle calculated from atmospheric reanalysis data (JRA-3Q) [22], the winter 2018 anomaly reached 1.0 × 10^{-6} m·s^{-1}, exceeding twice the seasonal variability of 4.6 × 10^{-7} m·s^{-1}, followed by a second maximum of 1.2 × 10^{-6} m·s^{-1} in winter

2021 (see Methods). These events coincided with a shift in the Aleutian Low (**Supplementary Fig. S4**), indicating an anomalous intensification of wind-driven upwelling.

Subsurface isopycnals shoaled concurrently, with the 26.50 σθ surface moving from approximately 150 m during 2014–2017 to 120 m after 2018 (**Fig. 4d**). The shoaling rates were comparable to the vertical displacement expected from the strengthened Ekman suction (**Supplementary Fig. S5**). MOBO-DIC showed a corresponding upward displacement of DIC-rich subsurface water, following the shoaling density structure (**Fig. 4e**).

These physical changes divide the post-2014 period into two stages: a subsurface carbon accumulation period (2014–2017) and a subsurface carbon release period (post-2018). During 2014–2017, enhanced stratification restricted winter diabatic exchange while the subsurface density structure remained relatively deep. Since 2018, strengthened Ekman suction shoaled the isopycnals while enhanced stratification persisted, providing a pathway for subsurface carbon to return toward the surface.

Winter CO_2 outgassing increased basin-wide since 2018 relative to the pre-2018 period by Northwest Pacific CO_2 flux map (NWP CO_2 flux map; **Fig. 5a**). The NWP CO_2 flux map is a high-resolution regional product that reconstructs surface DIC, total alkalinity, and pCO_2sea before calculating air–sea CO_2 flux [23] (see Methods). The climatological mean of NWP CO_2 flux map shows net outgassing across the Bering Basin (**Supplementary Fig. S6**), consistent with prior climatological observational study [24,25]. The positive outgassing anomaly extended across most of the Bering Basin, with the strongest increase occurring along northern coast (**Fig. 5a**), aligning with subsurface warming pattern identified in prior work [15]. The basin-wide pattern indicates that the post-2018 increase was not confined to the shelf or seasonal sea-ice coverage region (**Supplementary Fig. S7**).

The time series of winter CO_2 flux followed the same two-stage evolution identified from the physical field (**Fig. 5b**). In the pre-2014 baseline period, basin-integrated January–March winter outgassing averaged 0.090 ± 0.008 Gt·C·yr^{-1}. During the first stage (2014–2018), winter outgassing remained suppressed at 0.086 ± 0.021 Gt·C·yr^{-1}, which is comparable to the pre-2014 baseline but significantly lower than the subsequent release stage. Notably, this lower outgassing during 2014–2017 partly reflects an initial decline in 2014, when suppressed winter diabatic exchange reduced the upward supply of subsurface DIC to the surface.

In the second stage (post-2018), winter CO_2 outgassing increased to 0.157 ± 0.047 $Gt \cdot C \cdot yr^{-1}$, reaching 1.75 times the pre-2014 baseline. By 2024, outgassing further increased to 0.225 ± 0.050 $Gt \cdot C \cdot yr^{-1}$, approximately 2.4 times the baseline (**Fig. 5b**). This increase was accompanied by rising sea-surface nDIC and pCO_2sea (**Fig. 5b**), with a flux decomposition attributing the acceleration primarily to the rise in pCO_2sea (**Supplementary Fig. S8**).

The correspondence between the physical and CO_2-flux stages suggests that the post-2018 outgassing increase was likely driven by renewed vertical exchange. As defined as DIC accumulating layer, the 26.50 σθ surface intersected the wintertime mixed-layer every year during pre-2014 baseline period (**Fig. 5c**). During 2014–2017, the accumulation period, this surface deepened to approximately 150 m, while the wintertime mixed-layer reached only about 120 m, preventing entrainment. Since 2018, the 26.50 σθ surface shoaled again, returning within reach of the wintertime mixed-layer and resuming winter exchange with the DIC accumulating layer.

The subsurface and surface nDIC records show the same transition. During the pre-2014 baseline period, nDIC on the 26.50 σθ surface from MOBO-DIC and winter surface nDIC from the NWP CO_2 flux map remained comparable (**Fig. 5d**). During the 2014–2017 accumulation period, subsurface nDIC increased while surface nDIC remained lower, producing a clear divergence between the two layers. Since 2018, the two records intersected again as the 26.50 σθ surface re-entered the wintertime mixed-layer. This convergence supports re-entrainment of the accumulated subsurface carbon into the winter surface, which likely elevated surface nDIC, increasing pCO_2sea and accelerating winter CO_2 outgassing.

The magnitude of the nDIC increase is also consistent across independent datasets. Surface nDIC from the NWP CO_2 flux map increased by approximately 36.0 $\mu mol \cdot kg^{-1}$ between 2007 and 2024. The P14 observations showed a 37.4 $\mu mol \cdot kg^{-1}$ nDIC increase between 2007 and 2023 (from 2274.6 ± 11.7 to 2312.0 ± 7.5 $\mu mol \cdot kg^{-1}$). The close agreement in magnitude, despite differences in absolute nDIC among the datasets, supports the subsurface reservoir as the source of subsequent surface carbon enrichment.

Together, strengthened Ekman suction, isopycnal shoaling, wintertime mixed-layer re-entrainment, and nDIC convergence resolve the release stage of accelerated outgassing. Carbon that accumulated below the wintertime mixed-layer after 2014 was re-entrained since 2018, elevating surface DIC and accelerating winter CO_2 outgassing to the atmosphere.

3. Summary and Discussions

This study identifies a multi-year accumulation-and-release pathway for carbon in the Bering Basin. Freshening-enhanced stratification suppressed winter water-mass renewal from early 2010s [15], retaining heat and biologically derived carbon in the subsurface (**Fig. 6a, b**). Sustained carbon supply led to DIC accumulation around 26.50 σθ layer, forming a DIC accumulating layer (**Fig. 6b**). Strengthened Ekman suction since 2018 shoaled the subsurface density layers, facilitating re-entrainment into the wintertime mixed-layer (**Fig. 6c**). This re-entrainment likely elevated surface DIC and pCO_2sea, accelerating winter CO_2 outgassing. Changes in winter water-mass renewal thus controlled carbon retention and the timing of its subsequent atmospheric release.

Importantly, this subsurface accumulation does not require increased biological productivity. Before 2014, annual winter mixing repeatedly entrained carbon to the surface, preventing multi-year buildup. Suppressed winter renewal removed this reset, allowing continued carbon supply below the surface. This mechanism is supported by the dominance of the AOU-derived soft-tissue component, reflecting prolonged isolation without increased primary production. Furthermore, the negative contributions post-2014 from solubility indicates that warming opposed, rather than caused, the carbon enrichment. A simple Bering Sea Carbon Outgassing Potential (BS-COP) index further demonstrates the physical coherence of this accumulation-and-release mechanism based on changes in wintertime mixed-layer and isopycnal depths (**Supplementary Fig. S9**). Biological export thus supplied the carbon, while restricted winter mixing drove its retention.

The residual nevertheless cannot be interpreted as a closed local carbon budget. The AOU-based soft-tissue estimate reflects both remineralization and circulation changes, while lateral DIC transport and productivity variations may modulate accumulation. In addition, the basin-wide surface CO_2 record is reconstructed rather than obtained from continuous direct measurements. The agreement among P14 observations, MOBO-DIC, and the NWP CO_2 flux map supports the inferred accumulation-and-release sequence but does not directly trace carbon from the subsurface to the atmosphere. Numerical simulations with ocean biogeochemical models are therefore required to further elucidate the mechanisms of enhanced CO_2 outgassing.

301 The post-2018 acceleration of winter CO_2 outgassing is regionally distinct, with the
302 Bering Basin standing out as the only North Pacific region exhibiting accelerated outgassing
303 in the NWP CO_2 flux map (**Supplementary Fig. S6**), likely associated with weakened winter
304 renewal. Similar delayed responses may occur in other high-latitude oceans. In the Southern
305 Ocean, enhanced wind-driven upwellings was expected to increase CO_2 outgassing, yet the
306 anticipated weakening of the carbon sink has not been observed [7,26–28]. Oliver and Haumann
307 (2025) [7] attributed this discrepancy to surface freshening, which enhanced stratification and
308 prevented DIC-rich upwelled water from reaching the atmosphere. The Bering Basin further
309 demonstrates that such subsurface carbon retention is not necessarily permanent
310 (**Supplementary Fig. S10**). Further strengthened Ekman suction can shoal accumulated
311 carbon toward the wintertime mixed layer. More broadly, this accumulation-and-release
312 mechanism creates a multi-year carbon-cycle memory, in which the atmospheric release of
313 regenerated carbon is delayed until physical connectivity is restored. Future numerical studies
314 should therefore resolve wintertime mixed-layer development, subsurface water-mass renewal,
315 and their responses to freshwater and atmospheric forcing.

316

4. Data and Methods

4.1 Data

4.1.1 P14 Line biogeochemical observations

This study uses three occupations of the GO-SHIP/WOCE P14 meridional section along the Date Line across the Bering Basin: the 1993 WOCE P14N cruise (R/V *Thomas G. Thompson*, July–September 1993) [18], the 2007 JAMSTEC revisit (R/V *Mirai*, October–November 2007) [17], and the 2023 JAMSTEC occupation (R/V *Mirai*, October–November 2023) [16] (**Supplementary Fig. S1**). All three occupations collected full-depth CTD/rosette profiles of temperature, salinity, and dissolved oxygen, together with bottle samples for nutrients (nitrate, phosphate, silicate), DIC, total alkalinity, and pH. CFC-12 was measured during the 1993 occupation and SF_6 during the 2023 occupation, providing the tracer constraints for the TTD analysis. No chemical tracer was available for 2007. DIC was measured coulometrically with certified reference material (CRM) calibration, yielding duplicate precision of ~1.2 ± 1.1 μmol·kg^{-1}, consistent with GO-SHIP target accuracies. Only data with quality flag 2 were used. All hydrographic variables were computed following TEOS-10. Biogeochemical and hydrographic properties were linearly interpolated onto isopycnal surfaces at 0.1 kg·m^{-3} intervals. Basin-mean profiles were formed by area-weighting all stations north of the 200 m isobath within the Bering Basin.

4.1.2 Oceanic objective analysis (ProjD)

ProjD is a global ocean temperature and salinity objective analysis on a 1° × 1° grid with 28 depth levels to 3000 m [20]. This study used the period 1990–2024. Hydrographic properties were converted to TEOS-10 variables and interpolated onto isopycnal surfaces. Mixed layer depth was defined as the shallowest depth where potential density exceeds the 10 m reference value by 0.125 kg·m^{-3}, and was area-averaged over the Bering Basin. To separate thermal and haline contributions to density variability, density was recomputed holding either salinity or temperature fixed at its climatological seasonal cycle while allowing the other to vary.

4.1.3 Data-constrained machine-learning DIC product (MOBO-DIC)

The Mapped Observation-Based Oceanic Dissolved Inorganic Carbon product (MOBO-DIC_MPIM) provides monthly DIC fields from 2004 to 2019 on a 1° × 1° grid with 28 vertical levels to 1500 m [19]. The product uses a self-organizing map feed-forward neural network (SOM-FFN) approach, with uncertainty quantified via bootstrap resampling (global mean uncertainty ~7 μmol·kg^{-1}). DIC was area-averaged over the Bering Basin and mapped to isopycnal surfaces using the density fields from ProjD.

4.1.4 Northwest Pacific CO_2 flux dataset (NWP CO_2 flux map)

The Northwest Pacific regional ocean CO_2 flux product, produced by Japan Meteorology Agency, provides monthly fields of surface DIC, total alkalinity, pCO_2sea, sea–air CO_2 flux, and related variables on a 0.25° × 0.25° grid over the northwest Pacific (15–67°N, 105°E–155°W) from 1998 to 2024 [23]. Surface DIC and total alkalinity are reconstructed via multiple linear regressions using satellite-derived sea surface temperature, sea surface salinity, sea surface dynamic height, chlorophyll-a, and mixed layer depth. Sea–air CO_2 flux is then calculated from the difference between oceanic pCO_2sea and atmospheric pCO_2air using the bulk formula with the gas transfer velocity parameterization of [29]. The global methodology is documented in Iida et al. (2021) [23]; a formal description of the regional product is in preparation.

To diagnose which variable drives the flux changes, we decomposed the CO_2 flux by allowing one variable at a time (pCO_2sea, gas exchange coefficient, or pCO_2air) to vary at its monthly value while holding the others fixed at their climatological seasonal cycle (**Supplementary Fig. S8**). Basin-integrated winter (January–February–March) CO_2 flux was computed by summing grid-cell fluxes weighted by spherical cell areas over all cells within the 200 m isobath of the Bering Basin.

4.2 Methods

4.2.1 Transit-time distribution method

Transit-time distribution (TTD) method was applied to estimate the anthropogenic contribution; the remaining DIC change was then evaluated as a potential natural-origin component. This approach treats seawater as a continuous mixture of water parcels with

varying ages, each carrying a distinct anthropogenic carbon burden acquired at the time of last surface contact [30–32]. The age distribution is parameterized as an inverse Gaussian distribution:

$$g(t) = \sqrt{\frac{\Gamma^3}{4\pi\Delta^2 t^3}}\, exp\left(\frac{-\Gamma(t-\Gamma)^2}{4\Delta^2 t}\right)$$

where Γ is the mean transit time and Δ is the width of the distribution, representing the degree of mixing. This study adopted Δ = Γ as the reference case, following Waugh et al. (2003) [31]. For full derivation, see **Supplementary Text 1**.

The mean transit time Γ was constrained using transient tracer observations. For the 1993 occupation, CFC-12 measurements were used as the tracer constraint. For the 2023 occupation, SF_6 was used, as CFC-12 atmospheric concentrations have plateaued and can no longer resolve young water mass ages. No chemical tracer was available for the 2007 occupation, precluding TTD-based decomposition for that year. For each station and density level, Γ was determined by matching the observed tracer concentration to the value predicted by convolving the atmospheric tracer history with the TTD.

Atmospheric tracer histories were converted to equilibrium surface-water concentrations using temperature- and salinity-dependent solubility functions. CFC-12 solubility was calculated following [33], whereas SF_6 solubility followed [34]. The resulting equilibrium tracer histories were convolved with the inverse-Gaussian TTD, and the mean transit time Γ was determined by minimizing the difference between calculated and observed tracer concentrations. The atmospheric CO_2 history was converted to equilibrium surface DIC using CO2SYSv3 with the same carbonate-system constant set described in Section 4.2.2.

Anthropogenic carbon (DIC_{ant}) was then estimated by convolving the TTD with the time history of equilibrium DIC increase driven by the rise in atmospheric CO_2, following the method of Waugh et al. (2006) [32] . Natural climate variability carbon (DIC_{nat}) was obtained from the residual: $DIC_{nat} = \Delta DIC_{total} - DIC_{ant}$, where ΔDIC_{total} is the total DIC difference between the two occupations.

Because the width-to-mean ratio (Δ/Γ) of the transit-time distribution cannot be constrained by a single transient tracer, its influence on the partition was assessed by repeating the full decomposition across Δ/Γ = 0.5, 1.0, 1.5, and 2.0, spanning advection-dominated to

strongly mixed regimes. For each ratio, the mean age Γ was re-fitted to the observed tracer under that ratio with Δ = (Δ/Γ). Γ applied consistently in both the age-fitting and the carbon convolution steps), and the anthropogenic and natural components were recomputed. The natural-origin fraction of the 1993-to-2023 DIC increase remained between 70% and 73% across this range (DIC_{nat} = 39.8–41.7 μmol·kg^{-1}; DIC_{ant} = 15.1–16.9 μmol·kg^{-1}; **Supplementary Fig. S3**). This insensitivity arises because the assumption biases the 1993 and 2023 anthropogenic estimates in the same direction, so its effect largely cancels in their difference. The value Δ/Γ = 1 [31], representing substantial mixing appropriate for the intermediate-depth Bering Basin, was adopted for the reported values.

4.2.2 Decomposition of natural carbon into biological and solubility pump contributions

The natural-origin DIC increase (DIC_{nat}), obtained as the residual after subtracting anthropogenic carbon from the total DIC change, was further decomposed into contributions from the biological pump and the solubility (physical) pump. All calculations were performed on isopycnal surfaces interpolated at 0.1 kg·m^{-3} intervals from 24.0 to 29.0 σθ, using data from the Bering Basin stations (north of 52°N on the P14 line).

The soft-tissue biological pump contribution was estimated from apparent oxygen utilisation (AOU). For each station and isopycnal surface, AOU was calculated as:

$$AOU = O_2^{sat}(S, \theta) - O_2^{obs}$$

where O_2^{sat} is the oxygen saturation concentration computed from absolute salinity and potential temperature using the Gibbs SeaWater (GSW) toolbox [35], and O_2^{obs} is the observed dissolved oxygen concentration. AOU represents the cumulative oxygen consumed by remineralisation of organic matter since the water parcel was last ventilated at the surface. AOU was converted to a carbon equivalent using the Redfield stoichiometric ratio of $C:O_2$ = 117:170 [36]:

$$C_{bio} = AOU \times \frac{117}{170}$$

The soft-tissue biological pump contribution to the DIC change between two occupations was then obtained as the difference:

$$\Delta C_{bio} = C_{bio}^{2023} - C_{bio}^{1993}$$

This term reflects the combined effects of organic matter remineralization and any changes in circulation or ventilation that alter the oxygen history of the water masses. The same calculation was applied to the 2007 occupation to obtain the 2007-to-1993 biological pump difference.

The hard-tissue biological pump contribution, reflecting the dissolution of calcium carbonate, was estimated from the change in total alkalinity relative to a preformed alkalinity baseline [37] . Preformed alkalinity (TA_{pre}) was derived from a local conservative temperature–salinity–alkalinity relationship rather than a global relationship, because global preformed-alkalinity formulations mis-specify the freshwater endmember of the Bering Basin and, given the basin's freshening, do not cancel in the inter-occupation difference. A linear TA–S_P (total alkalinity–practical salinity) relationship was fitted to the conservative (pre-dissolution) portion of the P14 observations, defined as water within the 25.50–26.20 σθ range where carbonate dissolution is negligible, pooled across all three occupations:

$$TA_{pre} = a \cdot S_p + b$$

with *a*=58.5 and *b*=306.6 (n = 195, R^2 = 0.83). Per-occupation fits gave slopes of 51–60 that were not statistically distinguishable given their standard errors and identical salinity ranges, so a single pooled relationship was adopted; the slope spread is carried as uncertainty. All salinities were converted to Practical Salinity (based on TEOS-10) for consistency with the alkalinity formulation.

The hard-tissue carbon (C_{hard}) was then computed as half the excess measured alkalinity (TA_{obs}) over the preformed value, corrected for the alkalinity change from nitrate release during organic-matter remineralisation:

$$C_{hard} = \frac{1}{2}(TA_{obs} - TA_{pre} + \Delta NO_3)$$

where ΔNO_3 = AOU × R(N:O_2), with R(N:O_2) = 0.125. On the 26.50 σθ surface, the preformed-alkalinity term reflects along-isopycnal salinification: although the upper ocean freshened, salinity on this fixed isopycnal increased between occupations, because density-compensated warming on a fixed density surface requires a compensating salinity increase. The hard-tissue contribution between occupations was obtained as $\Delta C_{hard} = C_{hard}^{2023} - C_{hard}^{1993}$, and analogously for 2007.

The solubility pump contribution isolates the thermodynamic effect of temperature and salinity changes on CO_2 solubility, independent of biological or anthropogenic influences. For each isopycnal surface, equilibrium DIC was calculated using CO2SYSv3 for MATLAB [38,39]. Calculations used the total pH scale, the first and second carbonic-acid dissociation constants (K_1 and K_2) of Lueker, Dickson, and Keeling (2000) [40], the bisulfate dissociation constant (KSO_4) of [41], the HF dissociation constant of Perez et al. (1987) [42], and the total boron–salinity relationship of Lee et al. (2010) [43]. Total alkalinity, silicate, and phosphate were held at the 1993 observed values for both years, while atmospheric pCO_2 was fixed at the preindustrial value of 280 μatm since the anthropogenic carbon is splited. Only temperature and salinity were allowed to vary between occupations:

$$C_{phys}^{1993} = f(Alk_{1993}, pCO_2 = 280, T_{1993}, S_{1993}, Si_{1993}, PO4_{1993})$$

$$C_{phys}^{2023} = f(Alk_{1993}, pCO_2 = 280, T_{2023}, S_{2023}, Si_{1993}, PO4_{1993})$$

where f denotes the DIC computed from CO_2 system thermodynamics at zero pressure (surface equilibrium). The solubility pump contribution was then:

$$\Delta C_{phys} = C_{phys}^{2023} - C_{phys}^{1993}$$

By fixing alkalinity, nutrients, and atmospheric pCO_2, any difference in the resulting DIC reflects purely the effect of temperature and salinity changes on CO_2 solubility. A negative ΔC_{phys} indicates that warmer subsurface temperatures reduced CO_2 solubility, decreasing the equilibrium DIC. The same procedure was applied to the 2007 occupation to obtain the 2007-to-1993 solubility pump difference.

A minor surplus (4.14 μmol·kg^{-1}), defined as $\Delta C_{surplus} = \Delta DIC_{nat} - \Delta C_{bio} - \Delta C_{phys}$, accounts for processes not captured by the AOU-based biological pump or the solubility calculation, potentially including lateral transport of carbon into or out of the basin.

Basin-averaged profiles and their spatial standard deviations were computed across all Bering Basin stations for each isopycnal surface. Values reported in the main text correspond to the 26.50 σθ surface, where both the subsurface warming and DIC enrichment were most pronounced.

4.2.3 Wind stress and Ekman velocity

Wind stress was computed from 10 m wind components of the JRA-3Q atmospheric reanalysis (1998–2024) [22] using the bulk formula with the drag coefficient parameterization [44]. Monthly wind stress curl was calculated from the resulting stress fields. Ekman vertical velocity (w_{ek}) was then estimated as:

$$W_{ek} = \frac{1}{\rho_0} \nabla \times \frac{\tau}{f}$$

where ρ_0 is a reference seawater density and f is the planetary vorticity. Positive values indicate Ekman suction (upwelling), negative values indicate Ekman pumping (downwelling). Basin-averaged Ekman velocity anomalies were computed after removing the 1998–2022 seasonal cycle.

4.2.4 Bering Sea Carbon Outgassing Potential (BS-COP) index

To test the physical coherence of the proposed accumulation-and-release mechanism showing that the variations of wintertime mixed layer and isopycnal layers can result in carbon accumulation in productive high-latitude seas, this study constructed a simple diagnostic index, the Bering Sea Carbon Outgassing Potential (BS-COP). This index is driven by only two input variables: the monthly depth of the 26.5 σθ isopycnal ($Z_{26.5}$) and the monthly wintertime mixed layer depth (Z_{WML}), both derived from the ProjD objective analysis.

The index couples two processes: subsurface carbon accumulation and winter re-entrainment. Carbon accumulates in the subsurface at a rate set by the biological pump (R_{bio} = 3.51 μmol·kg^{-1}·yr^{-1}, as derived from the seasonal cycle analysis). Each winter, the accumulated reservoir is partially depleted if the mixed layer penetrates the isopycnal, and simultaneously, a fraction of the reservoir is re-exposed to the atmosphere. The outgassing potential in any given year is the product of the two: how much carbon has accumulated, and how much of it is re-exposed during winter.

The subsurface carbon reservoir R_t evolves annually as:

$$R_t = (R_{t-1} + R_{bio}) \cdot exp(-k_{rest} \cdot P_{max})$$

where P_{max} is the maximum mixed layer penetration depth beyond the isopycnal during the winter ($P_{max} = \max(Z_{WML} - Z_{26.5}, 0)$ over January–April). The exponential decay term represents the renewal of the carbon-accumulating layer by deep winter mixing: when the

mixed layer penetrates well past the isopycnal (large P_{max}), most of the reservoir is ventilated and reset. When the mixed layer does not reach the isopycnal ($P_{max} = 0$), the reservoir is preserved and grows by R_{bio}.

The winter re-exposure of the reservoir is quantified by a monthly exposure fraction e_m, averaged over the four winter months (January–April):

$$e_m = 1 - exp[-(k_{re} \cdot S_m + k_{cont} \cdot P_m)]$$

where $S_m = \max(d_{ref} - Z_{26.5}, 0)$ is the shoaling distance of the 26.5 σθ surface above a reference depth (d_{ref} = 140 m, representing the typical isopycnal depth during the accumulation period), and $P_m = \max(Z_{WML} - Z_{26.5}, 0)$ is the direct penetration of the mixed layer past the isopycnal in month m. The parameter k_{re} controls the sensitivity to isopycnal shoaling (e.g., by Ekman suction), while k_{cont} provides an additional contribution when the mixed layer physically contacts the carbon-accumulating layer. The winter-mean exposure $\bar{e}$ is the average of e_m over January–April.

The BS-COP index is then:

$$BSCOP = R_t \times \bar{e}$$

This formulation captures the two-stage mechanism identified in this study. During the accumulation period (2014–2017), $P_{max} \approx 0$ and $\bar{e} \approx 0$: the reservoir grows but is not re-exposed, producing near-zero outgassing anomalies. After 2018, strengthened Ekman suction reduces $Z_{26.5}$, increasing both S_m (shoaling exposure) and P_m (mixed layer contact). The reservoir, now laden with years of accumulated carbon, is partially re-entrained, producing elevated BS-COP values.

The parameter values (k_{re} = 0.045, k_{cont} = 0.03, k_{reset} = 0.012) were tuned to reproduce the observed subsurface carbon reservoir (~35 μmol·kg^{-1} by 2023) and the timing of the outgassing acceleration after 2018. Anomalous outgassing is defined as BS-COP − R_{bio}, representing the departure from the baseline annual biological carbon input.

References

1. Freeman, E., Skinner, L. C., Waelbroeck, C. & Hodell, D. Radiocarbon evidence for enhanced respired carbon storage in the Atlantic at the Last Glacial Maximum. *Nat. Commun.* **7**, 11998 (2016).

2. Skinner, L. C. *et al.* Radiocarbon constraints on the glacial ocean circulation and its impact on atmospheric CO2. *Nat. Commun.* **8**, 16010 (2017).

3. Baker, C. A., Martin, A. P., Yool, A. & Popova, E. Biological Carbon Pump Sequestration Efficiency in the North Atlantic: A Leaky or a Long-Term Sink? *Global Biogeochem. Cycles* **36**, (2022).

4. Miura, T., Suga, T. & Hanawa, K. *Winter Mixed Layer and Formation of Dichothermal Water in the Bering Sea*. *Journal of Oceanography* vol. 58 https://link.springer.com/article/10.1023/A:1022871112946 (2002).

5. Miura, T., Suga, T. & Hanawa, K. *Numerical Study of Formation of Dichothermal Water in the Bering Sea*. *Journal of Oceanography* vol. 59 (2003).

6. Fogaren, K. E. *et al.* Winter Mixing Controls Carbon Sequestration by the Biological Pump in the Subpolar North Atlantic. *J. Geophys. Res. Oceans* **131**, (2026).

7. Olivier, L. & Haumann, F. A. Southern Ocean freshening stalls deep ocean CO2 release in a changing climate. *Nat. Clim. Chang.* **15**, 1219–1225 (2025).

8. Springer, A. M., Peter McRoy, C. & Flint, M. V. The Bering Sea Green Belt: Shelf-edge processes and ecosystem production. *Fish. Oceanogr.* **5**, 205–223 (1996).

9. Mizobata, K., Wang, J. & Saitoh, S. Eddy-induced cross-slope exchange maintaining summer high productivity of the Bering Sea shelf break. *J. Geophys. Res. Oceans* **111**, (2006).

10. Mathis, J. T., Cross, J. N. & Bates, N. R. Coupling primary production and terrestrial runoff to ocean acidification and carbonate mineral suppression in the eastern Bering Sea. *J. Geophys. Res.* **116**, C02030 (2011).

11. Dubinina, E. O., Kossova, S. A., Chizhova, Yu. N. & Avdeenko, A. S. Dissolved Inorganic Carbon (δ13C(DIC), [DIC]) in Waters of the Western Bering Sea. *Oceanology (Wash. D. C).* **64**, 681–694 (2024).

12. Fransson, A., Chierici, M. & Nojiri, Y. Increased net CO_2 outgassing in the upwelling region of the southern Bering Sea in a period of variable marine climate between 1995 and 2001. *J. Geophys. Res. Oceans* **111**, (2006).

13. Stabeno, P. J. & Hristova, H. G. Observations of the Alaskan Stream near Samalga Pass and its connection to the Bering Sea: 2001-2004. *Deep. Sea. Res. 1. Oceanogr. Res. Pap.* **88**, 30–46 (2014).

14. Ladd, C. Seasonal and interannual variability of the Bering Slope Current. *Deep. Sea. Res. 2. Top. Stud. Oceanogr.* **109**, 5–13 (2014).

15. Shu, H.W. *et al.* Abrupt basin-wide subsurface warming in the Bering Sea since 2014 revealed by in-situ monitoring observations. *J. of Oceanography* (2026).

16. Katsumata, K. *R/V Mirai Cruise Report MR23-07*. (2023).

17. Kawano, T. & Murata, A. *MR07-06 Cruise Report*. (2007).

18. WOCE Hydrographic Programme, W. Hydrochemistry measured on water bottle samples during Thomas G. Thompson cruise 325023_1 on section P14N [dataset]. Preprint at (2002).

19. Keppler, L., Landschützer, P., Lauvset, S. K. & Gruber, N. Recent Trends and Variability in the Oceanic Storage of Dissolved Inorganic Carbon. *Global Biogeochem. Cycles* **37**, (2023).

20. Ishii, M. & Kimoto, M. Reevaluation of historical ocean heat content variations with time-varying XBT and MBT depth bias corrections. *J. Oceanogr.* **65**, 287–299 (2009).

21. Rodionov, S. N., Bond, N. A. & Overland, J. E. The Aleutian Low, storm tracks, and winter climate variability in the Bering Sea. *Deep Sea Research Part II: Topical Studies in Oceanography* **54**, 2560–2577 (2007).

22. KOSAKA, Y. *et al.* The JRA-3Q Reanalysis. *Journal of the Meteorological Society of Japan. Ser. II* **102**, 2024–004 (2024).

23. Iida, Y., Takatani, Y., Kojima, A. & Ishii, M. Global trends of ocean CO2 sink and ocean acidification: an observation-based reconstruction of surface ocean inorganic carbon variables. *J. Oceanogr.* **77**, 323–358 (2021).

24. Takahashi, T. *et al.* Global sea–air CO2 flux based on climatological surface ocean pCO2, and seasonal biological and temperature effects. *Deep Sea Research Part II: Topical Studies in Oceanography* **49**, 1601–1622 (2002).

25. Takahashi, T. *et al.* Climatological mean and decadal change in surface ocean pCO2, and net sea–air CO2 flux over the global oceans. *Deep Sea Research Part II: Topical Studies in Oceanography* **56**, 554–577 (2009).

26. Anderson, R. F. *et al.* Wind-Driven Upwelling in the Southern Ocean and the Deglacial Rise in Atmospheric CO $_2$. *Science (1979).* **323**, 1443–1448 (2009).

27. Pan, X. L., Li, B. F. & Watanabe, Y. W. Intense ocean freshening from melting glacier around the Antarctica during early twenty-first century. *Sci. Rep.* **12**, 383 (2022).

28. Spence, P. *et al.* Rapid subsurface warming and circulation changes of Antarctic coastal waters by poleward shifting winds. *Geophys. Res. Lett.* **41**, 4601–4610 (2014).

29. Wanninkhof, R. Relationship between wind speed and gas exchange over the ocean revisited. *Limnol. Oceanogr. Methods* **12**, 351–362 (2014).

30. Waugh, D. W., Haine, T. W. N. & Hall, T. M. Transport times and anthropogenic carbon in the subpolar North Atlantic Ocean. *Deep Sea Research Part I: Oceanographic Research Papers* **51**, 1475–1491 (2004).

31. Waugh, D. W., Hall, T. M. & Haine, T. W. N. Relationships among tracer ages. *J. Geophys. Res. Oceans* **108**, (2003).

32. Waugh, D. W., Hall, T. M., McNeil, B. I., Key, R. & Matear, R. J. Anthropogenic CO_2 in the oceans estimated using transit time distributions. *Tellus B: Chemical and Physical Meteorology* **58**, 376 (2006).

33. Warner, M. J. & Weiss, R. F. Solubilities of chlorofluorocarbons 11 and 12 in water and seawater. *Deep Sea Research Part A. Oceanographic Research Papers* **32**, 1485–1497 (1985).

34. Bullister, J. L., Wisegarver, D. P. & Menzia, F. A. The solubility of sulfur hexafluoride in water and seawater. *Deep Sea Research Part I: Oceanographic Research Papers* **49**, 175–187 (2002).

35. McDougall, T. J. & Barker, P. M. *Getting Started with TEOS-10 and the Gibbs Seawater (GSW) Oceanographic Toolbox*. vol. SCOR/IAPSO WG127 (2011).

36. Anderson, L. A. & Sarmiento, J. L. Redfield ratios of remineralization determined by nutrient data analysis. *Global Biogeochem. Cycles* **8**, 65–80 (1994).

37. Feely, R. A. *et al.* In situ calcium carbonate dissolution in the Pacific Ocean. *Global Biogeochem. Cycles* **16**, (2002).

38. van Heuven, S., Pierrot, D., Rae, J., Lewis, E. & Wallace, D. W. R. CO2SYS v 1.1, MATLAB program developed for CO2 system calculations. *ORNL/CDIAC-105b. Carbon Dioxide Information Analysis Center, Oak Ridge National Laboratory, U.S. DoE, Oak Ridge, TN.* (2011).

39. Sharp, J. D. *et al.* CO2SYSv3 for MATLAB (Version v3.2.1). Preprint at (2021).

40. Lueker, T. J., Dickson, A. G. & Keeling, C. D. Ocean pCO2 calculated from dissolved inorganic carbon, alkalinity, and equations for K1 and K2: validation based on laboratory measurements of CO2 in gas and seawater at equilibrium. *Mar. Chem.* **70**, 105–119 (2000).

41. Dickson, A. G. Standard potential of the reaction: , and and the standard acidity constant of the ion HSO4− in synthetic sea water from 273.15 to 318.15 K. *J. Chem. Thermodyn.* **22**, 113–127 (1990).

42. Perez, F. F. & Fraga, F. Association constant of fluoride and hydrogen ions in seawater. *Mar. Chem.* **21**, 161–168 (1987).

43. Lee, K. *et al.* The universal ratio of boron to chlorinity for the North Pacific and North Atlantic oceans. *Geochim. Cosmochim. Acta* **74**, 1801–1811 (2010).

44. Large, W. G. & Pond, S. Open Ocean Momentum Flux Measurements in Moderate to Strong Winds. *J. Phys. Oceanogr.* **11**, 324–336 (1981).

Acknowledgements: We would like to express our gratitude to the captains, officers, and crew of the R/V *Mira*, as well as the leading researchers, particularly Dr. Takeshi Kawano and Dr. Katsuro Katsumata. We also thank Dr. Kentaro Honda, Dr. Tomoki Sato, Dr. Shunpei Sato and Dr. Tomonori Azumaya for their previous long-term hydrographic observations in the Bering Sea. Dr. Ichiro Yasuda, Dr. Tomonori Azumaya, Dr. Kentaro Honda, Dr. Takashi Obase, Dr. Takahiro Toyota and Dr. Akio Yamakami provide the insightful comments to this study. The author HWS also expresses his gratitude to JD. Eric Wang and Dr. Hugo Huang for language advice as well as HC. Soichiro Tate, HC. Aaron Angelo and HC. Daniel Tallman for their support.

This study was supported by the Japan Society for the Promotion of Science under KAKENHI Grant Numbers JP22H05207 (MacroCoast) and JP24K22913, as well as World Premier International Research Center Initiative (WPI), MEXT, Japan, and also the Collaborative Research Program of the Research Institute for Applied Mechanics, Kyushu University (2026CR-AO-21).

Author Contributions: HWS, HT, SO and SK designed and constructed the study. YI provides the NPW CO_2 flux map dataset and decomposition method. AM and HWS apply and discuss TTD method and soft-tissue, hard-tissue biological pumps. SO, SK and HWS discuss the contribution of biological pump. SY and HWS discuss the solubility pump. SY and HWS discuss the CO_2 flux change and its validation. SK and HWS discuss the wind stress curl. HT, SK, SK, SO and HWS discuss the re-entrainment mechanism. HWS and AM review the prior studies regarding to impacts of enhanced stratification. SY, SO, SK, SK, HT and HWS discuss the structure and hypothesis of this study. HWS performs all the analysis and figures. HWS prepared the first draft of manuscript, and with all authors revised in second edition. All authors provide their opinion and contribute to this study substantially.

Competition interests: Authors declare that they have no competing interests.

Data and Materials availability:

All data for P14 Line observations are available at: (i) 1993: https://epic.awi.de/id/eprint/29281/1/Rod1993a.pdf , (ii) 2007: https://cchdo.ucsd.edu/cruise/49NZ20071008 , and (iii) 2023: https://cchdo.ucsd.edu/cruise/49NZ20231006

ProjD are publicly available from JMA at: https://climate.mri-jma.go.jp/pub/ocean/ts/v7.3.1/

All data from the MOBO-DIC_MPIM distribution are available at: https://catalog.data.gov/dataset/mapped-observation-based-oceanic-dissolved-inorganic-carbon-monthly-fields-from-2004-through-20

All data for JRA-3Q are available at: https://jra.kishou.go.jp/JRA-3Q/index_en.html

All NWP CO2 flux dataset all are available at: https://www.data.jma.go.jp/kaiyou/english/co2_flux/co2_flux_data_en.html

Code availability:

TTD method

Soft-tissue biological pump

Hard-tissue biological pump

BS-COP Index

(Codes will be provided through Code Ocean system)

Figures

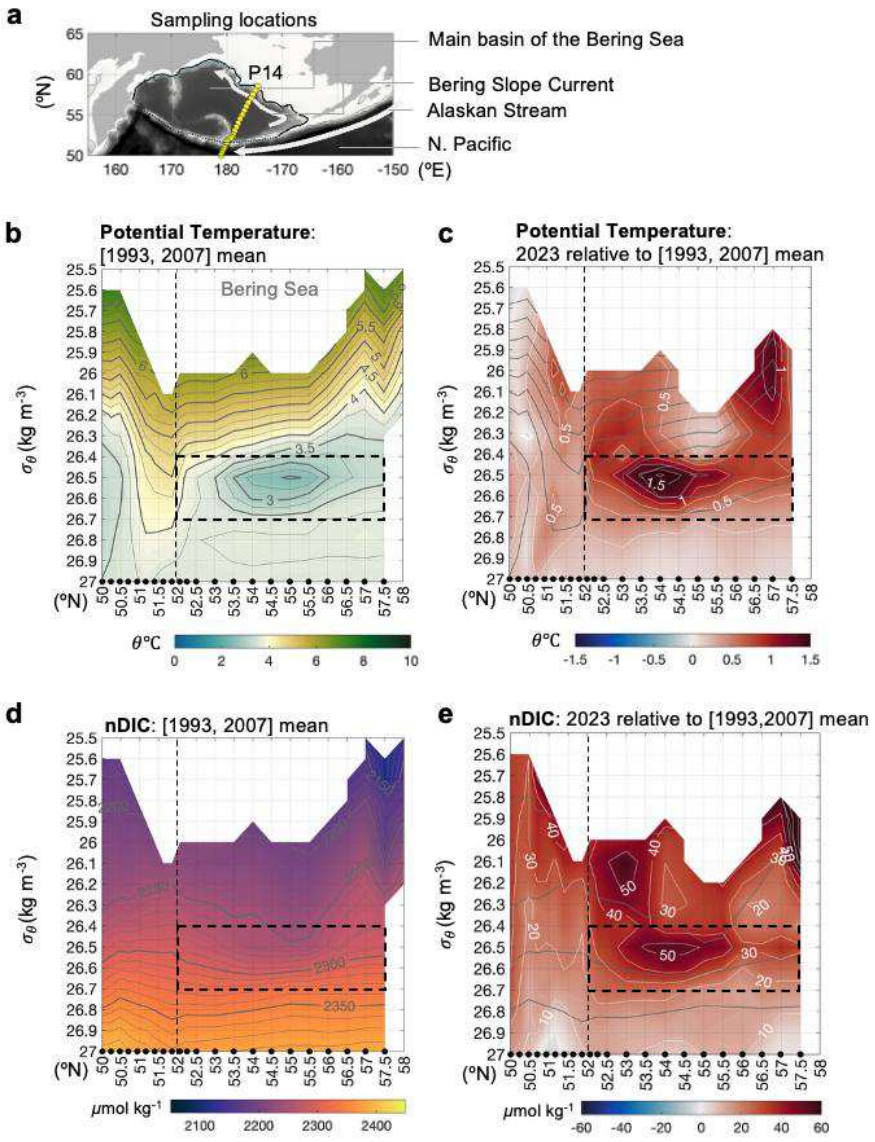
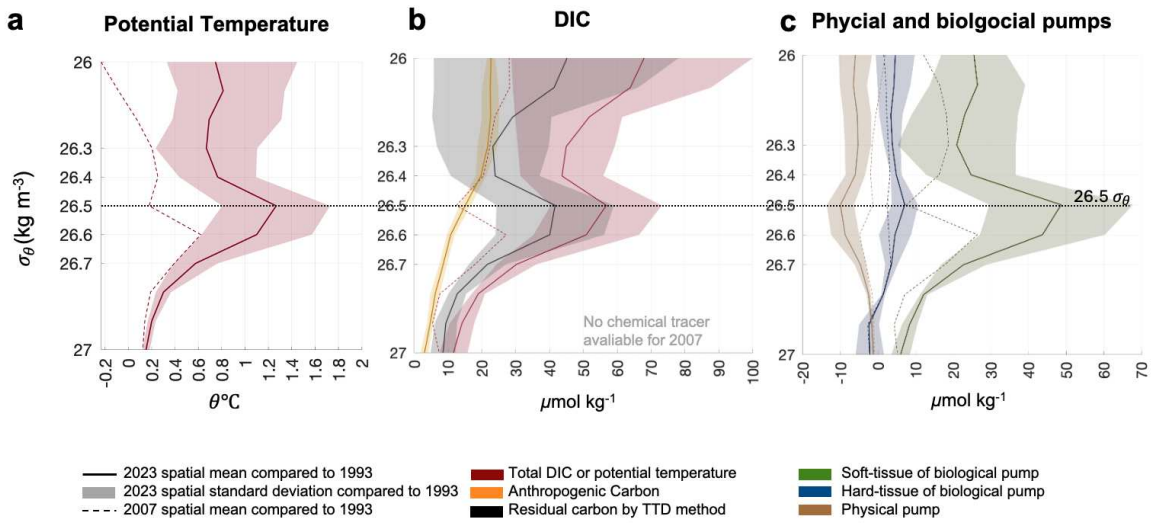


Figure 1. Observational evidence of subsurface warming and increased nDIC in the Bering Sea. **a.** Sampling locations along P14 line (yellow dots) across the Bering Basin, delineated by 200 m isobaths (black line, continusely with dashed-line across the Aleutian Straits). Gray lines denote 1000 m isobaths and 200 m isobaths outside of Bering Basin. Light-grey arrows represent the path of Alaskan Stream and Bering Slope Current. **b.** Mean potential temperature derived from 1993 and 2007 observations in density coordinate. Grey contours denote 0.5 ºC intervals, and black dots indicate sampling latitudes. The Bering Basin region is located north of the vertical dashed black line. Dashed-box encircles the remant of wintertime mixed layer between 26.40–26.70 σθ. **c.** Potential temperature differences in 2023 relative to the [1993, 2007] mean. White contours highlight these differences at 0.5 ºC intervals, with grey

708 contours representing the [1993, 2007] mean as reference. **d.** As in panel (b), but for nDIC.
709 Grey contours denote nDIC concentrations at 10 μmol·kg^{-1} intervals. **e.** As in panel (c), but for
710 nDIC. White contours highlight the nDIC differences at 10 μmol·kg^{-1} intervals.

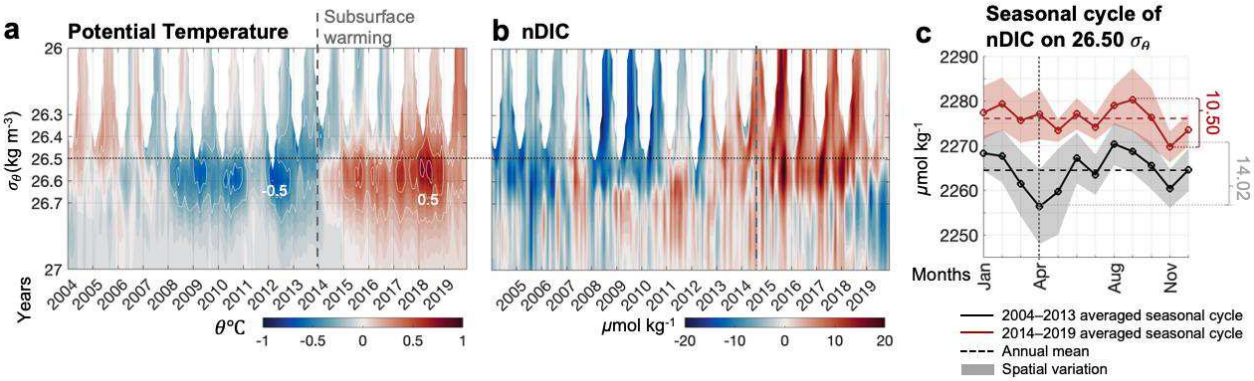
711



712

713 **Figure 2. Decomposition of increased DIC. a.** Basin-averaged temperature differences in
714 density coordinate from 2023 to 1993 (solid red line, shade as spatial standard deviation) and
715 2023 to 2007 (dashed red line). **b.** Same as panel (a) but for DIC. Black and yellow lines denote
716 the increase of nDIC into anthropogenic component and the residual by TTD method with
717 shades as spatial standard deviations, respectively. Dashed red line denotes the differences of
718 total DIC in 2007 relative to 1993. **c.** Decomposition of increased DIC in 2023 into soft-tissue
719 biological pump (green line), hard-tissue biological pump (blue line) and solubility pump
720 (brown line). Shades denote the spatial standard deviation. Dashed lines represent the
721 decomposition of differences in DIC in 2007 compared to 1993.

722



723

724 **Figure 3. Time evolution of subsurface warming and increased DIC in density**
725 **coordinates. a.** Time series of basin-averaged temperature changes (ProjD) after removing
726 2004–2019 seasonal cycles. White contours emphasize the anomalies at 0.25 ºC intervals. **b.**
727 As in panel (a), but for nDIC derived from MOBO-DIC dataset. **c.** Seasonal cycle of nDIC on
728 the 26.50 σθ isopycnal for the 2004–2013 (black) and 2014–2019 (red) from MOBO-DIC
729 dataset. Shaded regions denote spatial variation, and dashed lines represent annual means. The
730 vertical line identifies the April minimum in 2014–2019. Values on the right indicate the annual
731 seasonal amplitude (maximum to minimum) for each period.

732

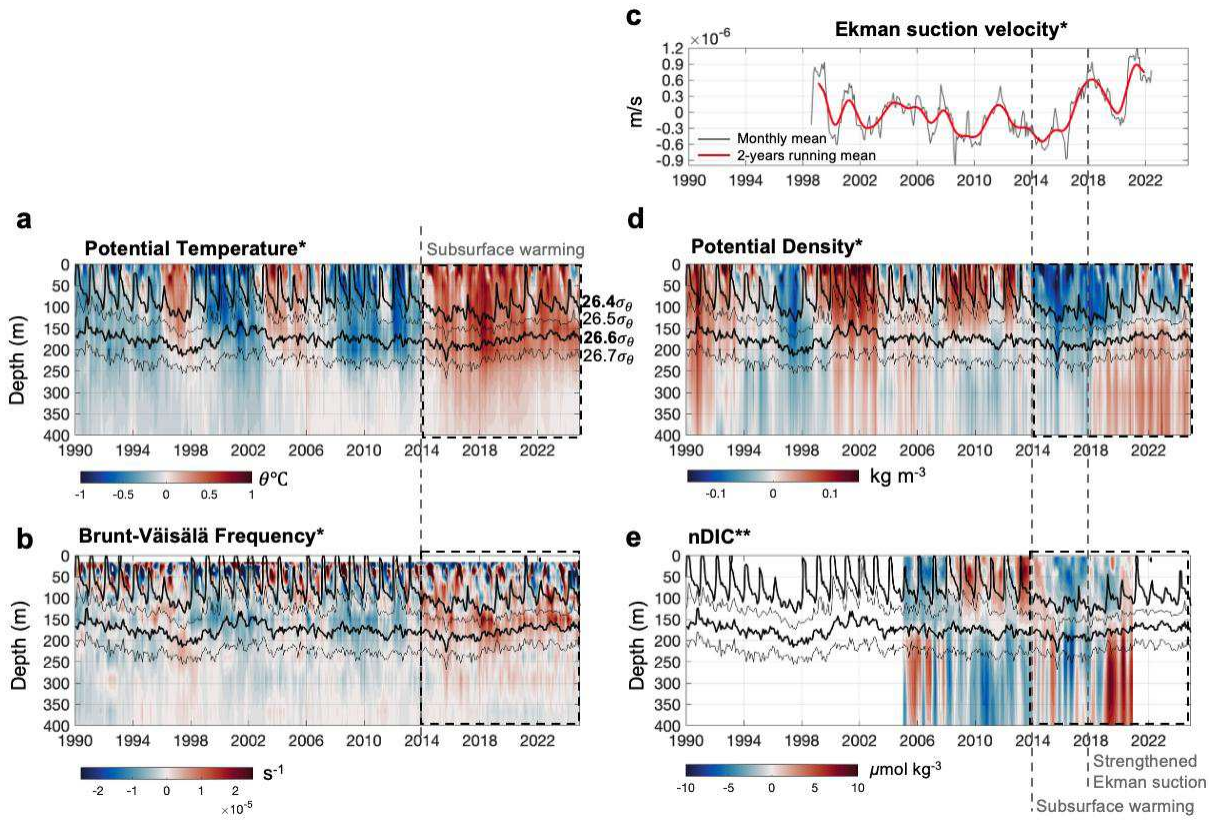
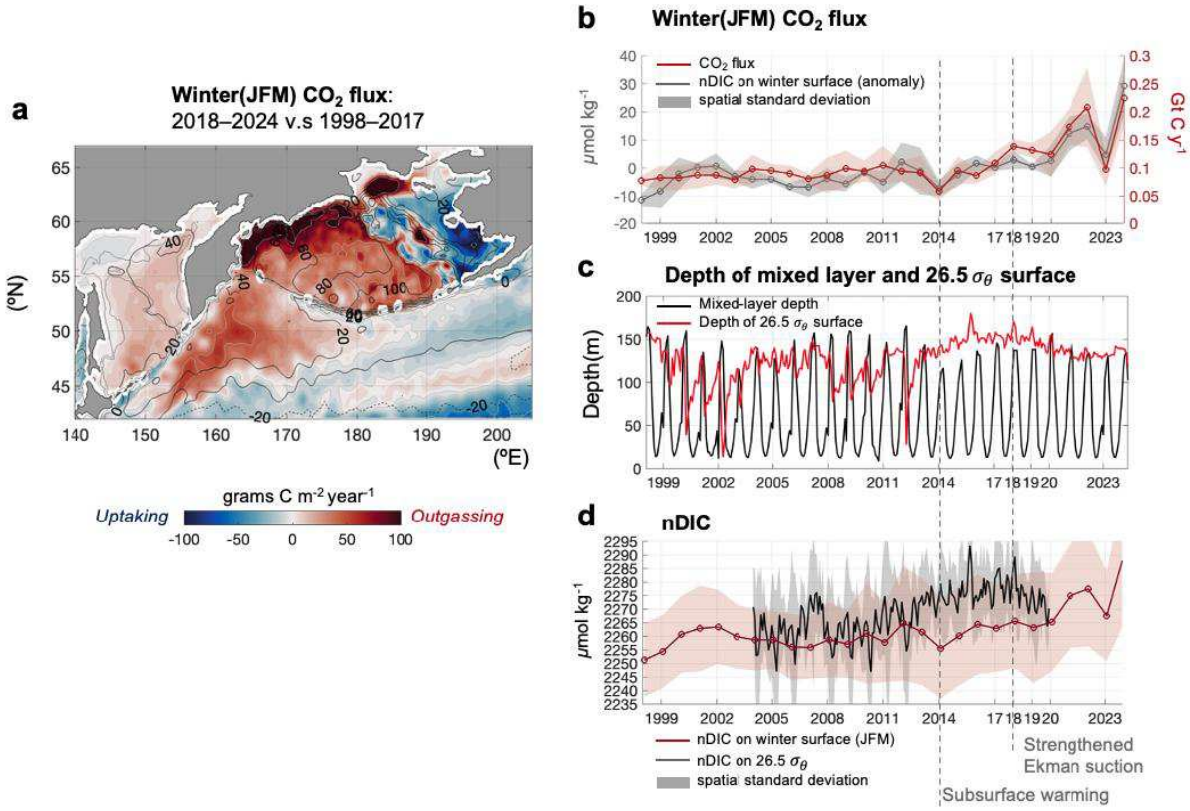


Figure 4. Enhanced stratification and upwelling of isopycnal surfaces by strengthened Ekman suction. a. Time series of basin-averaged temperature anomalies (ProjD) after removing the 1990–2024 seasonal cycles. Black contours denote selected isopycnals from 26.40 to 26.70 σθ. **b.** As in panel (a), but for Brunt-Väisälä frequency (N^2). **c.** Time series of basin-averaged monthly (grey line) and 2-years running mean (red line) of Ekman suction velocity anomalies (JRA3Q) after removing 1998–2022 seasonal cycle. **d.** As in panel (a), but for potential density anomalies. **e.** Time series of basin-averaged nDIC anomalies (MOBO-DIC) after removing 2004–2019 seasonal cycle.



743

744 **Figure 5. Accelerated CO_2 outgassing and the re-entrainment of the DIC accumulating**
745 **layer. a.** Winter (January-February-March) CO_2 flux anomalies (2018–2024) relative to the
746 1998–2017 mean from JMA regional CO_2 flux dataset; grey contours denote 20 grams C·m^{-3}·year^{-1}
747 intervals. Red shading represents the increase of outgassing. Black contours denote the
748 1998–2017 winter average. **b.**Time series of basin-integrated winter CO_2 outgassing (red line,
749 original value) and basin-averaged sea surface nDIC anomalies (black line, 1998–2024 mean
750 removed) estimated from JMA regional CO_2 flux dataset. Shading indicates spatial standard
751 deviation. **c.**Time series of basin-averaged mixed-layer depth (black) and the depth of 26.50
752 σθ surface (red) estimated from ProjD. **d.** Time series of nDIC on the winter sea surface
753 (January-February-March) from JMA regional CO_2 flux dataset (red) and on 26.50 σθ surface
754 from MOBO-DIC dataset (black). Shading indicates the spatial standard deviations.

755

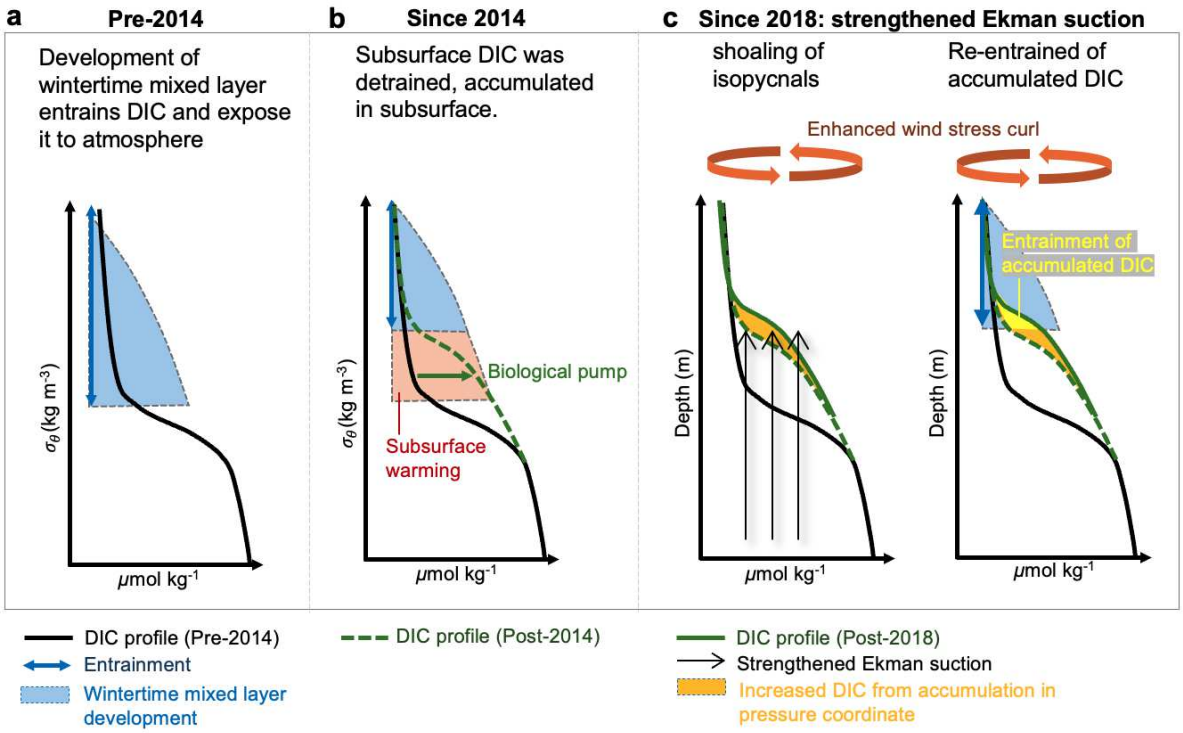


Figure 6. Proposed mechanism for the formation and atmospheric release of the DIC accumulating layer. a. Pre-2014, the development of wintertime mixed layer entrains the DIC-rich water, exposing to the atmosphere. **b.** Since 2014, restricted winter diabatic exchange process has enhanced stratification and induced subsurface warming. DIC was sequestered and accumulated in the subsurface via the soft tissue biological pump, forming a DIC accumulating layer. **c.** After 2018, strengthened Ekman suction shoaled this layer, facilitating its re-entrainment into the wintertime mixed-layer and accelerating CO_2 outgassing.

Supplementary Files

This is a list of supplementary files associated with this preprint. Click to download.

- SupplementaryFiguresfinal.docx
- SupplementaryText1TTDmethod.docx